IEEE Access
Multidisciplinary | Rapid Review | Open Access Journal

Received 30 August 2022, accepted 12 September 2022, date of publication 21 September 2022,
date of current version 30 September 2022.

Digital Object Identifier 10.1109/ACCESS.2022.3208378

RESEARCH ARTICLE

Channel Measurements and Characterizations for Long Range Air-to-Ground Communication Systems in the UHF Band

JAESIN KIM[1,2] AND INKYU LEE[1], (Fellow, IEEE)
[1]School of Electrical Engineering, Korea University, Seoul 02841, South Korea
[2]Defence Space Technology Center, Agency for Defense Development, Daejeon 34186, South Korea

Corresponding author: Inkyu Lee (inkyu@korea.ac.kr)

This work was supported in part by the National Research Foundation of Korea (NRF) through the Korea Government [Ministry of Science and ICT (MSIT)] under Grant 2022R1A5A1027646, and in part by the Core Technology Research and Development Project through the Korea Government [Defense Acquisition Program Administration (DAPA)] under Grant 912464301.

ABSTRACT In this paper, we consider long range air-to-ground (AG) communication systems which support aeronautical platforms including unmanned aerial vehicles (UAVs) in the ultra high frequency (UHF) band. For such a system, we present the measurement based path loss analysis and multipath characteristic results at the distance of hundreds of kilometers. To this end, the experimental AG channel measurement system is implemented at the aircraft with various ground station (GS) environments. Through realistic flight tests, we observe the path loss behaviors for long range UHF channels with sea and ground earth surface reflections. By comparing the measurement results with the empirical path loss model and the spherical earth two-ray model, we demonstrate that our measurement results match well with the model. Moreover, for the multipath channel characterization, we provide field test results on the occurrence probability, delay, and power of multipath components in hilly and mountainous environments with various altitudes of the aircraft.

INDEX TERMS Air-to-ground, long range communication systems, channel characterization, UHF band.

I. INTRODUCTION

In recent years, there have been a rapid growth in the use of unmanned aerial vehicles (UAVs) for various applications such as military reconnaissance and civilian airborne cellular networks [1], [2], [3], [4]. For such aerial systems, an air-to-ground (AG) communication link should be extremely reliable. In the UAV system operating within line-of-sight (LOS) region, the AG communication link can be classified into an wideband high capacity data link and a narrowband command and control (C2) data link. The first one indicates the AG wideband trunk that transmits radar, imagery, video, and other sensor information at high rates of hundreds of Mbps from the airborne platform to the ground station (GS), while the second one represents a link which sends and receives reliable C2 and telemetry messages for the UAV and its payload at the rate of lower than tens of Mbps via the AG wireless channel.

Due to the limitation of available spectrum, the wideband AG data link typically adopts high frequency bands such as X or Ku bands even though it suffers from a huge propagation loss [5]. Thus, it practically needs high-gain directional tracking antenna systems to cover hundreds of kilometers. However, the lower frequency bands such as ultra high frequency (UHF), L, and C have superiority over higher frequencies in terms of the reliability of the long range AG links, resulting from much less multipath fading, attenuation, phase distortion, and delay spread [6]. Normally, the UHF band enables to extend a coverage of the system, and it has been shown that atmospheric effects such as precipitation do not affect transmissions in the UHF band. These inherent characteristics provide competitive advantages in harsh applications. Thus, several military AG communications employ the UHF band for long range environments [7], [8].

The associate editor coordinating the review of this manuscript and approving it for publication was Julien Sarrazin.

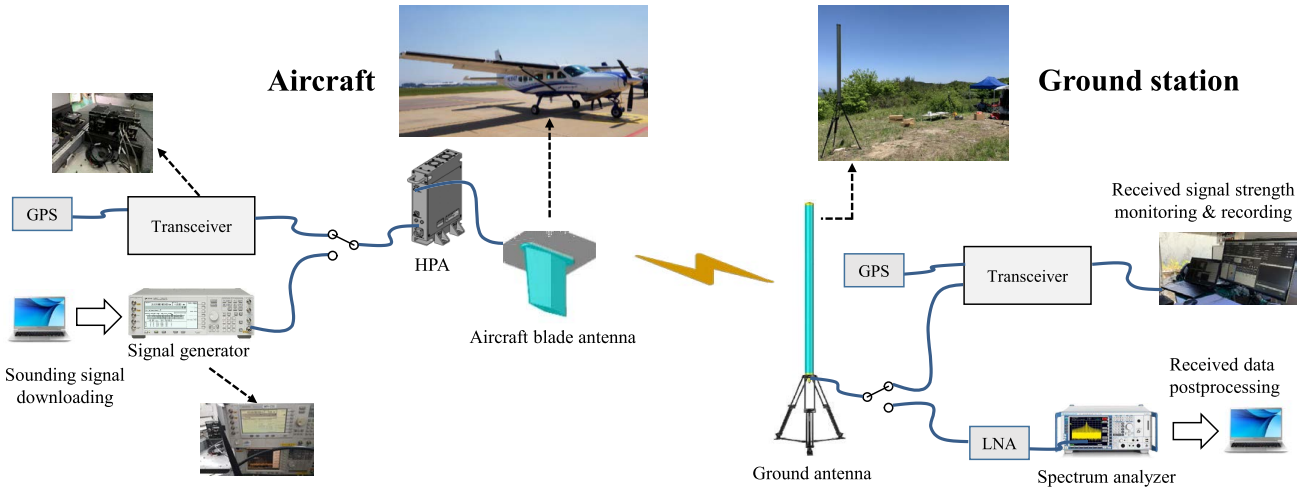

FIGURE 1. System configuration for long range AG channel measurements.

Signal propagation characteristics at various frequency bands have been studied through modeling and extensive measurements in various AG scenarios. To the best of our knowledge, no literature has investigated the measurement based path loss and multipath characteristics for long rage AG communication systems in the UHF band yet [9]. Authors in [10] presented the experimental results of AG channels with a sea surface at the C band over a range of 45 to 95 kilometers. Comprehensive AG channel models were developed and tested in [11], [12], and [13] under over-water, hilly/mountainous, and sub/near-urban scenarios for L and C bands with a link distance of less than 50 kilometers. Also, the works [14], [15], [16], [17], [18] focused on the low altitude channel in cellular networks or short range urban areas.

In [19], a flight measurement campaign for the L-band AG channel was presented together with results on the measured channel characteristics for positioning applications. A part of the channel measurement was performed at an aerial height up to 11 km and a link distance of 350 km. However, many papers are still limited in the AG channel with short coverage, and most field tests were conducted only at the distance of hundreds of meters. Furthermore, an elevation angle based two-ray path loss model with a varying reflection coefficient was proposed in [20] without field measurements. Authors in [21] generated a three-dimensional UAV-to-vehicle channel model by integrating a machine learning method under a typical urban scenario at 28 GHz. The AG channel exhibits distinct features compared to other terrestrial or urban communication channels. For more accurate prediction, the earth curvature based environments should be considered for long range AG communication systems. Therefore, the study on the AG channel involving actual tests is important for long range airborne platforms in the UHF band.

In this paper, we present field measurement results for the path loss and multipath characteristics in the long range AG communication environments. For measurements, we implement the experimental AG communication system in the UHF band at the aircraft and various GSs. We conduct flight measurement tests under realistic AG channel scenarios. Throughout the flight test, we focus on examining long range path loss behaviors with the sea and ground earth surface reflections. Additionally, for the multipath channel characteristic analysis, we investigate the occurrence probability of multipath component, delay, and power relative to the line-of-sight (LOS) component values in hilly and mountainous GSs. We demonstrate the measurement result to illustrate the multipath effects for different AG channel environments.

Main contributions of this paper include the followings: 1) long range AG path loss analysis for the sea and ground surface reflections, 2) measurement based spherical earth path loss model and log-distance path loss model, 3) multipath component statistics for various aircraft and GS settings, and 4) quantification of delay spread characteristics for long range AG multipath channels. Note that all measurements are conducted by actual flights in the UHF band.

The remainder of this paper is organized as follows: In Section II, we address a flight measurement setup to investigate the AG channel properties. Section III provides the measured path loss results with the sea and ground reflections including empirical losses predicted by models. Under various GS conditions, the observations of multipath effects are presented in Section IV, and conclusions are presented in Section V.

II. MEASUREMENT SETUP

In this section, we present the flight measurement setup for test campaigns which observe path loss and multipath channel characteristics. For measurements, we implement the experimental AG channel measurement system as shown in Fig. 1. It consists of a transceiver with UHF antennas, a high power amplifier (HPA), and the channel sounding configuration including a signal generator and a spectrum analyzer. For the path loss measurement, the transceiver continuously

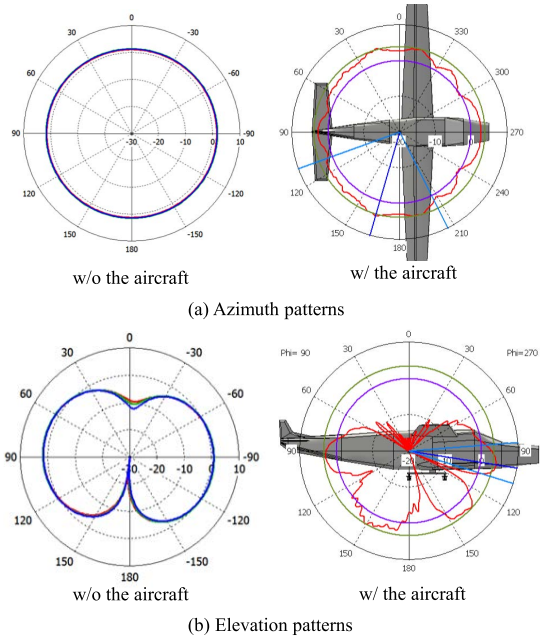

FIGURE 2. Comparison of the antenna radiation patterns for the cases with and without the aircraft.

transmits a signal with a bandwidth of 2 MHz and records the received signal strength according to the information of the global positioning system (GPS) installed on the aircraft. On the other hand, for the multipath measurement, the signal generator and the spectrum analyzer are utilized at the aircraft and the GS sides, respectively. When the noise or interference level increases, we additionally use a low noise amplifier (LNA) at the front-end of the spectrum analyzer in order to obtain a signal level above the noise floor.

For a safe and effective flight test, the manned aircraft Cessna 208 Caravan has been used in our experiment as shown in Fig. 1. In the aircraft configuration, most components are installed inside the aircraft, and the omni-directional blade antenna is mounted on the bottom surface of the aircraft. While the antenna is mounted on the fuselage, it impacts on the resulting radiation pattern. We analyze the whole radiation patterns based on a simplified aircraft computer-aided design (CAD) model. The radiation patterns with respect to the azimuth and elevation angles are plotted in Fig. 2. The figures show that some deviations with null patterns are found for the antenna mounted on the aircraft due to the effect of the fuselage. However, it would be sufficient to consider the aircraft antenna gain as 2 dBi in low elevation angle of interest. On the other hand, in the GS, we employ an omni-directional antenna with a length of 2.4 m and a gain of 7 dBi. Note that the antennas for both sides are vertically polarized.

In Fig. 3, we illustrate a block diagram on the channel sounding process which is essential for the multipath channel measurement. The channel sounding signal based on a spread spectrum technique is implemented at the vector signal generator of the aircraft. After acquiring channel impulse responses

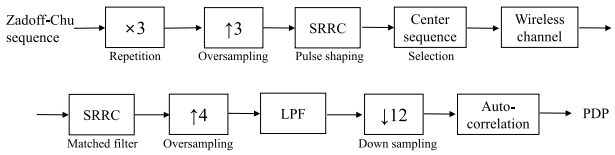

FIGURE 3. Processing block diagram of the channel sounding signal.

at the spectrum analyzer of the GS, the individual power delay profile (PDP) is generated in the postprocessing.

For the channel sounding input, we create a Zadoff-Chu seqeunce, which is well-known as a constant amplitude and zero auto-correlation sequence. This sequence usually provides good auto-correlation performance in many fields. The sounding signal is operated at a sampling clock of 14 MHz, which allows for a time resolution of 71.4 ns in the multipath measurement[1]. Then the sounding signal is filtered by a square root raised cosine (SRRC) response with the roll-off factor of 1.0. Unlike [11] with the roll-off of 0.3, we adopt a larger roll-off value in order to further reduce oscillations in the time domain. After passing through the target AG channel, the spectrum analyzer in the GS samples the received signal digitally. Finally, the PDPs are produced by the postprocessing that includes the SRRC filtering and the auto-correlation.

In the measurement setup, the center frequency is assigned between 400 and 500 MHz depending on spectrum availability. The flight speed is set to 270 to 300 km/h during all flights. The flight trajectories have been predefined such that clear radio LOS can be maintained in term of the antenna's field of view. An airframe shadowing may occur when the aircraft body itself obstructs the radio LOS toward the GS. We prevent such circumstances for the measurements by allowing only straight-and-level flights. The detailed environments about the GSs and the trajectories of aircraft will be described in Sections III and IV.

III. PATH LOSS ANALYSIS

In this section, we provide the path loss measurements for long range AG communication channels with both sea and ground surface reflections. Then we compare with results predicted by the international telecommunications union (ITU) recommended model and the spherical earth two-ray model. Here, we focus on the path loss analysis according to a distance between the aircraft and the GS, mainly from 100 to 200 km.

A. PATH LOSS MODEL DESCRIPTIONS

1) ITU-R P.528 MODEL

The path loss model can be divided into a site-general model and a site-specific model [6]. First, recommendation ITU-R

[1] While the delay between two paths is close to the time resolution of the measurement system, two paths are often unresolvable [22]. However, as discussed in [11], it is sufficient to identify most multipath components because the long range AG channel with a high altitude has a relatively sparse multipath environment.

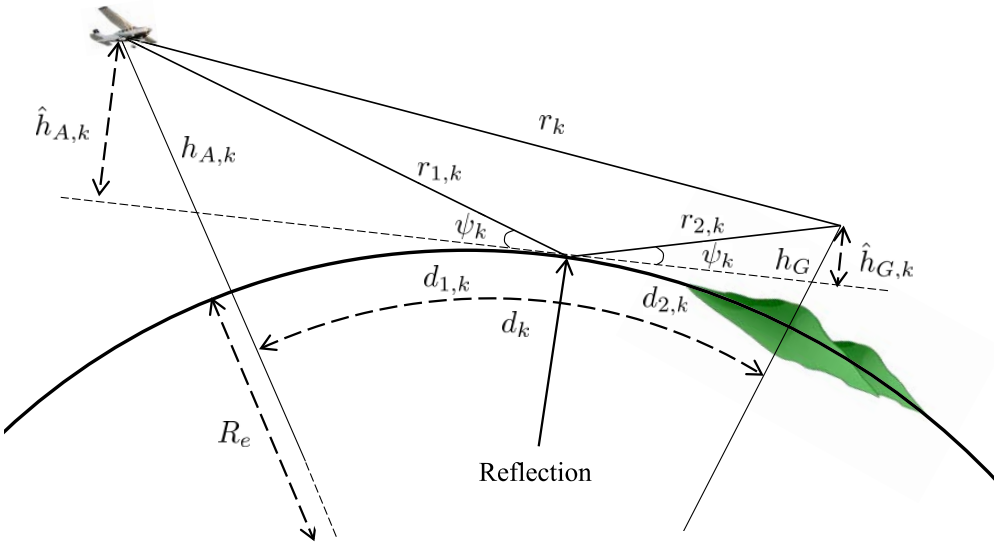

FIGURE 4. Geometry of the spherical earth over the two-ray path.

P.528 provides a basic path loss calculation method in the frequency range from 100 MHz to 30 GHz for aeronautical systems [23]. However, the P.528 model only assumes the smooth earth surface with a mean annual global reference atmosphere and sets a conductivity $\sigma = 0.005$ S/m and a relative dielectric constant $\epsilon_r = 15$ as the average ground surface. In addition, since the variability of the P.528 model is based on a considerable amount of experiment data obtained mainly for a continental temperate climate, it is close to a site-general model in such an environment.

To predict the path loss from the P.528 model, we need the heights of the aircraft antenna h_A and the GS antenna h_G above mean sea level (AMSL), the antenna parameter Θ indicating either horizontal or vertical linear polarization, and the desired time percentage t of the long-term variability as well as the distance d and the frequency f. The path loss of the P.528 model can be represented as L_{528} with these input parameters.

2) SPHERICAL EARTH TWO-RAY MODEL

If we take the spherical earth surface reflection into consideration, the path loss can be explained by a well-known two-ray model. The LOS path and the earth surface reflection are determined via a geometry, which means that the deterministic two-ray model is inherently site-specific. The path loss calculation for the spherical earth geometry starts with a two-ray model involving the phasor sum of the direct and the reflected rays. Since the actual field strength deviates from the flat earth model, we cannot expect to yield more realistic path loss results at large distances. Therefore, we offer in Fig. 4 the geometry of the spherical earth over the two-ray path and various parameters used in this paper.

To establish the spherical earth two-ray model, we first determine the geometrical specular reflection point located at the distance $d_{1,k}$ away form the aircraft, shown in Fig. 4. By introducing the time index k in the subscript, we represent variables that change with the movement of the aircraft. Since an exact model exists only for a flat earth assumption [24], an approximate solution is available for our long range situation with a small grazing angle. The great circle distance between the aircraft and the reflection point $d_{1,k}$ is given as [25]

$$d_{1,k} = \frac{d_k}{2} + p_k \cos\left(\frac{\Phi_k + \pi}{3}\right) \tag{1}$$

where $p_k = \frac{2}{\sqrt{3}}\sqrt{R_e(h_{A,k} + h_G) + d_k^2/4}$ and $\Phi_k = \cos^{-1}\left(2R_e(h_{A,k} - h_G)d_k/p_k^3\right)$. Hence, the remaining distance $d_{2,k}$ is derived as $d_{2,k} = d_k - d_{1,k}$. The effective earth radius R_e is defined as $R_e = \alpha R$ where α denotes the effective earth radius factor and the earth radius $R = 6371$ km.

In the terrestrial channel with radio waves traveling near the surface, the effective earth radius factor α is normally chosen as $4/3$ to account for the ray bending effect due to changes in the atmospheric refractivity. In our approach, the effective earth radius factor α can be obtained form the average radius of the curvature method proposed in [26]. However, since the overall effect against the altitude changes is negligible, α is set to 1.4 based on a constant surface refractivity of the test area.

The aircraft altitude, the GS antenna height and the slant range between the aircraft and the GS are denoted as $h_{A,k}$, h_G and r_k, respectively, which are known in advance. The value Δr_k denotes the difference between the direct slant range r_k and the length of the reflected ray $r_{1,k} + r_{2,k}$ as [27]

$$\begin{aligned}\Delta r_k &\triangleq r_{1,k} + r_{2,k} - r_k \\ &= d_k\left(\sqrt{1 + \frac{(\hat{h}_{A,k} + \hat{h}_{G,k})^2}{d_k^2}} - \sqrt{1 + \frac{(\hat{h}_{A,k} - \hat{h}_{G,k})^2}{d_k^2}}\right),\end{aligned} \tag{2}$$

where $\hat{h}_{A,k} = h_{A,k} - \frac{d_{1,k}^2}{2R_e}$ and $\hat{h}_{G,k} = h_G - \frac{d_{2,k}^2}{2R_e}$ mean the heights of the aircraft and the GS antennas above the plane tangent to the surface of the earth at the point of reflection, respectively. Note that $\hat{h}_{G,k}$ changes with $d_{2,k}$ unlike h_G. Also, the length of the direct path r_k is computed as $r_k = ((R_e+h_{A,k})^2+(R_e+h_G)^2-2(R_e+h_{A,k})(R_e+h_G)\cos(\frac{d_k}{R_e}))^{1/2}$, which is determined by the link geometry.

Now, the total received field strength at time k is given as

$$E_k = E_{d,k}F_k = E_{d,k}(1+\rho_k D_k P_k e^{-j\Delta\phi_k}) \tag{3}$$

where $E_{d,k}$ is the direct wave field strength, the path-gain factor $F_k = 1+\rho_k D_k P_k e^{-j\Delta\phi_k}$ means that how the field at the receiving antenna differs from $E_{d,k}$ [25], ρ_k denotes the surface reflection coefficient, D_k is the divergence factor, P_k is the partial reflection factor and $\Delta\phi_k$ indicates the relative phase difference according to Δr_k.

The coefficient ρ_k depends on the frequency, polarization, grazing angle ψ_k, and electrical constant at the surface reflection point. For our test case, a complex value ρ_k in the vertical polarization is given by

$$\begin{aligned}\rho_k &= |\rho_k|\, e^{\theta_k} \\ &= \frac{(\epsilon_r - j60\lambda\sigma)\sin\psi_k - \sqrt{(\epsilon_r - j60\lambda\sigma) - \cos^2\psi_k}}{(\epsilon_r - j60\lambda\sigma)\sin\psi_k + \sqrt{(\epsilon_r - j60\lambda\sigma) - \cos^2\psi_k}}\end{aligned} \tag{4}$$

where θ_k denotes the phase and ϵ_r, σ, λ and ψ_k represent a relative dielectric constant of the surface, a conductivity, a wavelength and a grazing angle, respectively [27]. Here, ψ_k is defined as $\psi_k = \hat{h}_{A,k}/d_{1,k} = \hat{h}_{G,k}/d_{2,k}$. When reflected from the earth surface, there is a reduction effect of the reflection coefficient geometrically arising from the divergence of the rays. This effect can be taken into account by rewriting the smooth spherical earth reflection coefficient as $\rho_k D_k$ where D_k is defined as [27]

$$D_k = \sqrt{1+\frac{2d_{1,k}d_{2,k}}{R_e(\hat{h}_{A,k}+\hat{h}_{G,k})}}. \tag{5}$$

From (2), we can obtain $\Delta\phi_k$ as $\Delta\phi_k = (2\pi/\lambda)\Delta r_k$. Also, P_k indicates the ratio of the reflected field strength from the non-uniform surface to that reflected by a uniform surface.

In [28], recommendation ITU-R P.525 contains popular methods to calculate the attenuation in free space between ideal loss-free isotropic antennas, which is referred to as free space path loss L_{fs}. The free space path loss is expressed as a function of the distance r_k and the frequency f as $L_{fs,k}(r_k, f)$. Also, $L_{a,k}$ denotes an adjustment factor for the average difference between the measured and the predicted path losses. It includes the environmental elements such as an additional atmospheric loss and imperfect electrical constants as well as small mismatches of the antenna gain influenced from some deviations of the flight trajectory. After converting (3) into the received power $P_{r,k}$ in a dB scale, $P_{r,k}$ is computed as

$$\begin{aligned}P_{r,k} &= P_T + G_T + G_R - L_C \\ &\quad - L_{fs,k} - L_{a,k} + 10\log_{10}|F_k|^2\end{aligned} \tag{6}$$

where P_T, G_T, G_R and L_C stand for a transmit power, a transmit antenna gain, a receive antenna gain, and total cable loss, respectively. Finally, the path loss L_k is given as

$$L_k = P_T + G_T + G_R - L_C - P_{r,k} \tag{7}$$

$$= L_{fs,k} + L_{a,k} - 10\log_{10}|F_k|^2 \tag{8}$$

$$\begin{aligned}&= L_{fs,k} + L_{a,k} \\ &\quad - 10\log_{10}\left|1+|\rho_k|\, D_k P_k e^{-j(\Delta\phi_k-\theta_k)}\right|^2\end{aligned} \tag{9}$$

$$\begin{aligned}&= L_{fs,k} + L_{a,k} - 10\log_{10}\Big((1+|\rho_k|\, D_k P_k)^2 \\ &\quad - 4|\rho_k|\, D_k P_k \sin^2(\frac{\theta_k - \Delta\phi_k}{2})\Big).\end{aligned} \tag{10}$$

3) LOG-DISTANCE MODEL BASED ON LEAST SQUARE CURVE-FITTING

Most of the measurements employ the log-distance path loss model where an increase in losses is represented by a value of the path loss exponent. The widely used log-distance path loss model against d_k is given as

$$\tilde{L}_k = A + 10n\log_{10} d_k \tag{11}$$

where $\tilde{L}_k$ is the log-distance path loss in dB, A represents a constant, and n indicates the path loss exponent [10]. Both n and A can be extracted from the measured data using a least square (LS) curve-fitting technique.

B. PATH LOSS MEASUREMENT RESULTS

In this subsection, we discuss on the received signal strength gathered at a distance between 100 and 200 km via several flights. Specially, we conduct two measurement campaigns in order to predict the path loss behavior on both sea and ground surfaces. To this end, we choose two GS locations such that the radio wave is mainly reflected over the sea or ground earth surfaces, which will be referred to as GS 1 and GS 2, respectively. GS 1 is located at about 1100 meters AMSL in an island area where can cause a sea water reflection. On the other hand, to establish the ground reflection environment, GS 2 is placed on an inland spot with about 900 meters AMSL. Note that both GSs are located in open fields surrounded by hilly and mountainous terrains as shown in Fig. 1. However, we can expect that the surface reflection effects are more dominant than terrains around the GS in terms of long range LOS path environments.

The flight tests are performed in the airspace of South Korea during spring and fall seasons. During several measurements, the weather conditions are clear and the sea is calm. By keeping the aircraft at an altitude of approximately 3.5 km within a distance of interest, the AG link can maintain a clear radio LOS channel. Under the predefined flight tracks, the flight trajectories are set straight toward or far away from each GS. Figure 5 shows the detailed measurement scenarios and trajectories in GS 1 and 2 under the LOS conditions. Prior to the measurement, we check the LOS coverage based on digital terrain elevation data.

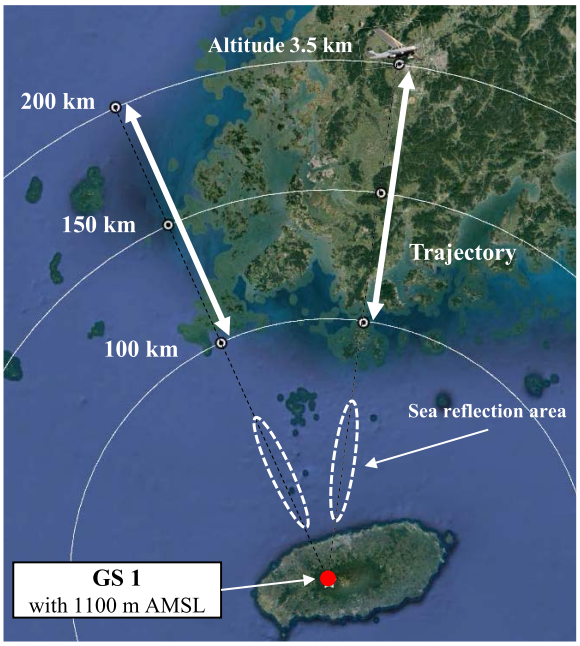

(a) Flight trajectory in GS 1 with the sea reflection

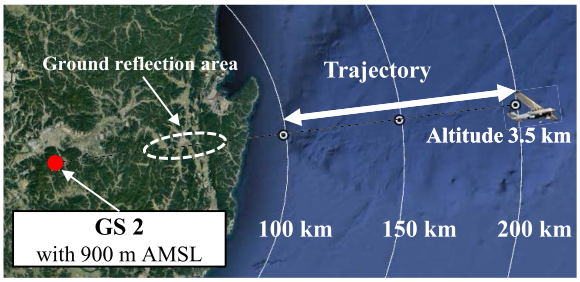

(b) Flight trajectory in GS 2 with the ground reflection

FIGURE 5. Flight trajectories in GS 1 and 2 under LOS conditions.

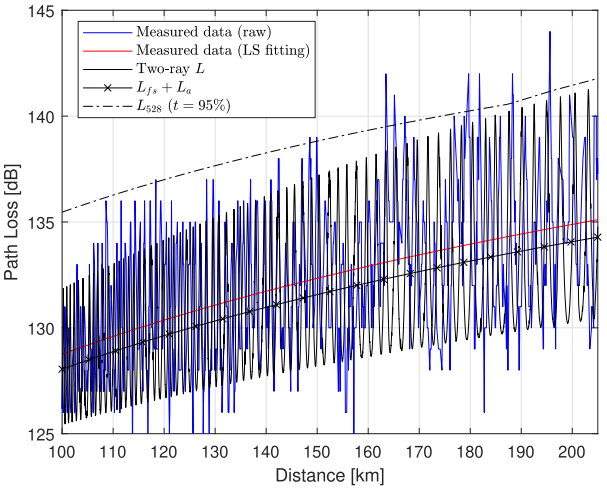

FIGURE 6. Path loss measurement in GS 1 with the sea reflection.

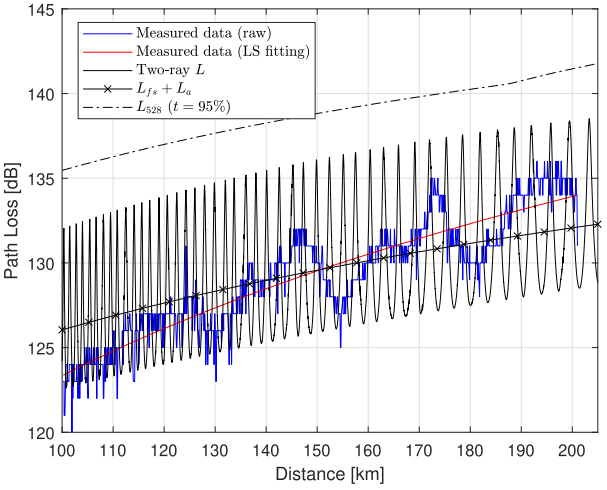

FIGURE 7. Path loss measurement in GS 2 with the ground reflection.

We now provide measurement results of the path loss. Figures 6 and 7 show the measured and predicted path loss results for the sea and ground surface reflection setting, respectively. The measured results generally follow a similar trend to the predicted results. We can see that the measurement result is reasonably well-approximated by the spherical earth two-ray model with the obtained parameters. The P.528 model path loss with $t = 95\%$ is plotted to compare with other graphs. Generally, the time percentage t of more than 95% is required to obtain more reliable AG communication service [23]. The statistics associated with the variability in the P.528 model represent the expected changes in the signal level over time. Hence, as can be seen in the figures, the P.528 model can serve as an upper bound in terms of the path loss of the AG link.

From the figures, we can check a periodic variation of the received power, which is a direct manifestation of the two-ray model. The reflected signal results in very deep fades pattern known as lobing. Typically, we can see more fluctuations due to measurement system variations and unexpected scattering such as surface condition[2]. Since the P.528 model belongs to the site-general model, it can provide a trend of the path loss based on general information rather than specific path parameters. In this regard, the P.528 model cannot account for the lobing effect because it omits the inclusion of detailed information such as the path-gain factor F_k according to the varying geometry of the two-ray path.

The lobing structure is highly dependent on surface characteristics such as roughness as well as electrical constants. Particularly, it is observed in Fig. 7 that the lobing pattern of the ground reflection case is not perfect compared to the sea reflection case of Fig. 6. Since the ground is a poorly reflecting surface relative to the signal wavelength, the ground reflection may be irregular or even not be present due to blocking from terrain obstructions. Also, since the sea is effectively smoother as the wavelength becomes longer, the two-ray lobing effect is more distinct compared to the

[2] Note that the measured data curves in Figures 6 and 7 are plotted with instantaneous and raw measurement data, even though the moving average results look smoother. For the link budget analysis of the AG system, we can utilize the practical fade depth of the lobing.

TABLE 1. Path loss model parameters.

Parameters	Smooth sea reflection (GS 1)	Suburban and hilly ground reflection (GS 2)
L_a	3 dB	1 dB
P	1	0.7
n	2.1	3.4
A	88.9	56.6

ground reflection condition. Moreover, we can recognize that the lobing effect becomes wider as the link distance increases.

For the spherical earth two-ray model, the reflection surface parameters related with the conductivity σ and the relative dielectric constant ϵ_r affect the fade depth of the lobes, whereas the interval of lobes is highly dependent on the aircraft altitude $h_{A,k}$. By plotting the model, we can observe that the interval of the lobes becomes narrow as $h_{A,k}$ increases. In the reflection coefficient computations (4), we assume a sea water with $\sigma = 5$ S/m and $\epsilon_r = 81$ and an average ground with $\sigma = 0.005$ S/m and $\epsilon_r = 15$ [27]. Although they may vary in practice, we keep them constant because their tiny changes do not significantly affect the path loss results. Likewise, we consider L_a and P as constants for simplicity. These model parameters are summarized in Table 1. Depending on where the reflection point is located at, we can encounter non-ideal surface situations. To deal with this problem, we adjust the two-ray model by using the partial reflection factor P. In the practical cases, P is found to have a value between 0.1 and 1.2 [24]. Also, L_a is an additional term derived from measurement environments. Therefore, model tuning is required for these two variables.

Based on the LS curve-fitting path loss model (11), the average path loss exponents along with the smooth sea and the suburban and hilly ground reflection points are calculated as 2.1 and 3.4, respectively, as shown in Table 1. The path loss exponent under the sea water reflection is close to that of the free-space. However, the ground reflection case has a higher path loss exponent compared to the sea water case. This is because the roughness of ground surface is not uniform as the reflection point varies. Because of the rugged terrains at ground reflection points, a weak ground reflection exists, whereas a strong sea reflection is likely to present due to the smooth sea surface.

IV. MULTIPATH CHANNEL CHARACTERISTICS

The multipath channel can be represented in terms of the complex channel impulse response $h(t, \tau)$. The PDP, which is proportional to $|h(t, \tau)|^2$, generally provides the received power at the receiver with a certain delay [17]. We thus calculate the instantaneous PDP for the kth received sequence as in Section II, which is defined as

$$\tilde{P}_k(\tau) = \sum_{i=1}^{N_k} |a_{k,i}|^2 \delta(\tau - \tau_{k,i}) \tag{12}$$

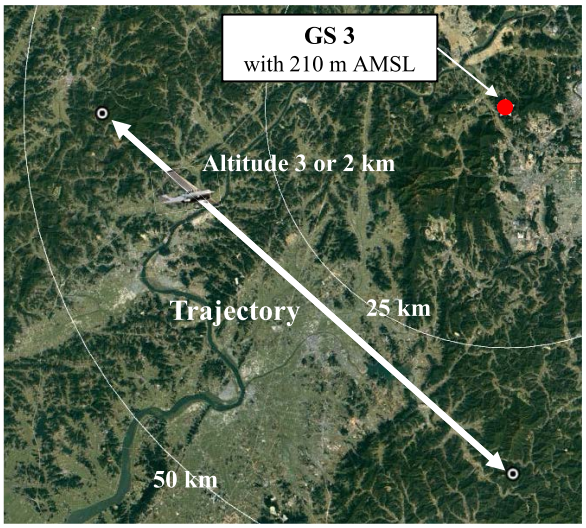

FIGURE 8. Flight trajectories in GS 3 under LOS conditions.

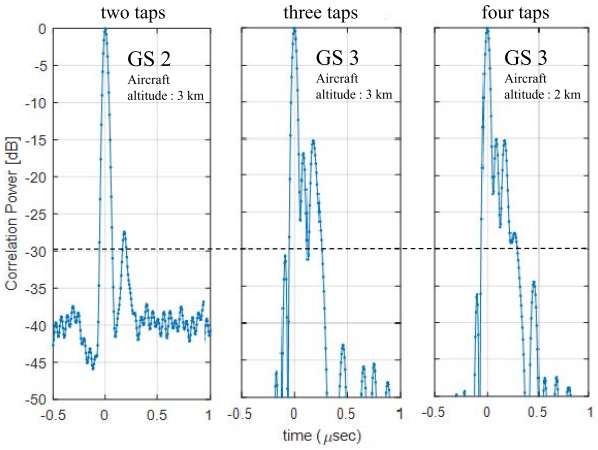

FIGURE 9. Snapshots of the PDPs with different taps in two hilly and mountainous GSs.

where $a_{k,i}$, $\tau_{k,i}$, and N_k denote the time-varying ith multipath component's amplitude, delay, and the number of multipath components at the kth time instant, respectively. In the following, we present field test results for the occurrence probability, delay, and power of multipath components in various AG communication environments.

By applying the channel sounding system described in Section II, the channel impulse responses are collected in an extra location GS 3 as well as GS 2 over more than one hour flight trial. Figure 8 shows the detailed measurement scenarios and trajectories in GS 3 under the LOS conditions. As stated in the previous section, although the pass loss behavior is similar to that of free space with a strong surface reflection, other multipath components from the sea water surface might be weaker [7], [11]. Hence, we discard GS 1 for this test case.

Finally, three typical scenarios are carried out. The GS 3 has a lower ground level of about 210 meters and a hilly and mountainous terrain with some small buildings compared to

TABLE 2. Quantification of multipath channel characteristics.

Ground	Aircraft	Metrics	1st tap	2nd tap	3rd tap	4th tap
GS 2 900 m AMSL	Altitude : 3 km above Range : 100-200 km	Occurrence probability [%]	93.03	6.57	0.4	-
		Average delay [ns]	0	93	185	-
		Average power [dB]	0	-24.16	-27.49	-
GS 3 210 m AMSL	Altitude : 3 km above Range : 30-40 km	Occurrence probability [%]	87.61	8.56	3.83	-
		Average delay [ns]	0	102	205	-
		Average power [dB]	0	-19.77	-12.31	-
	Altitude : 2 km below Range : 30-40 km	Occurrence probability [%]	58.13	27.34	10.42	4.11
		Average delay [ns]	0	143	184	224
		Average power [dB]	0	-27.51	-21.69	-22.13

GS 2. For this reason, we can expect a more dispersive environment in the GS 3. After the postprocessing, we obtain the instananeous PDPs of (12) by aligning the channel impulse responses so that the direct LOS component has zero delay and unit power. Figure 9 shows snapshots of the instantaneous PDPs with different multipath components, which are measured in GS 2 and 3 with different scenarios. The second multipath components are mainly generated due to reflections on the ground surface with suburban and hilly features. Especially, small buildings around the GS 3 under the hilly and mountainous environment might be a potential source of intermittent third and fourth multipath components.

For the quantitative statistical analysis, the occurrence probability, averaged delay, and averaged power of each multipath component in different GS environments are summarized in Table 2. In such a analysis, we ignore taps with power 30 dB lower than the first tap [15], [29], [30]. In other words, the criterion for determining the multipath tap is set to more than -30 dB as represented in Fig. 9. The results obviously show that the multipath effects gradually become more serious in GS 3 compare to GS 2 in spite of a large elevation angle in the GS 3 geometry setting. This is because some buildings near GS 3 generate more rich scattering. Also, as expected, the number of multipath components N_k and the occurrence probability of the third component significantly increase as the altitude of the aircraft decreases.

It was observed in [11] and [12] that the occurrence probability of the third ray becomes lower as the link distance increases, whereas the delay is not highly dependent on the link distance. Note that the delay characteristic is a fairly weak function of the frequency and link distance. Likewise, the experiment result on GS 2 over long range exhibits a similar delay trend while it has a very low probability of the third component occurrence.

Furthermore, the root mean squre (RMS) delay spread is calculated based on multipath components in average PDPs. The RMS delay spread in GS 2 is found to be 9.7 ns, while for GS 3, we obtain the RMS delay spread of 23.6 ns and 47.5 ns at the altitude of 2 km and 3 km, respectively. Despite higher altitude, the test with the altitude of 3 km has a larger RMS delay spread since it receives stronger multipath signals in the second and third taps as shown in Table 2.

V. CONCLUSION

In this paper, we have addressed the experimental characterization and the modeling of the long range AG communication channel over the sea and ground at the UHF band. The measured path loss has been compared with the predicted losses based on the spherical earth two-ray model and the ITU recommended model. The path loss analysis results have suggested that the measured losses follow a similar trend to that predicted by our two-ray model. In addition, the multipath characteristic results have shown that the multipath component exist in the long range AG channel on a fairly high probability regardless of their sparse and intermittent property. The results are important to design the long range AG communication system of the UAV for modern military and civilian airborne network applications.

ACKNOWLEDGMENT

An earlier version of this paper was presented in part at the APISAT, Gold Coast, Australia, December 2019 [DOI: 10.3316/informit.9781925627404].

REFERENCES

[1] C. Yan, L. Fu, J. Zhang, and J. Wang, "A comprehensive survey on UAV communication channel modeling," *IEEE Access*, vol. 7, pp. 107769–107792, 2019.

[2] A. Baltaci, E. Dinc, M. Ozger, A. Alabbasi, C. Cavdar, and D. Schupke, "A survey of wireless networks for future aerial communications (FACOM)," *IEEE Commun. Surveys Tuts.*, vol. 23, no. 4, pp. 2833–2884, 4th Quart. 2021.

[3] S. Eom, H. Lee, J. Park, and I. Lee, "UAV-aided wireless communication designs with propulsion energy limitations," *IEEE Trans. Veh. Technol.*, vol. 69, no. 1, pp. 651–662, Jan. 2020.

[4] S. Eom, H. Lee, J. Park, and I. Lee, "UAV-aided two-way mobile relaying systems," *IEEE Commun. Lett.*, vol. 24, no. 2, pp. 438–442, Feb. 2020.

[5] J. Kim, J. Lee, and I. Lee, "Antenna tracking techniques for long range air-to-ground communication systems using a monopulse method," *IEEE Access*, vol. 8, pp. 166442–166449, 2020.

[6] A. W. Graham, N. C. Kirkman, and P. M. Paul, *Mobile Radio Network Design in the VHF and UHF Bands*, 1st ed. Hoboken, NJ, USA: Wiley, 2007.

[7] W. Khawaja, I. Guvenc, D. W. Matolak, U. Fiebig, and N. Schneckenburger, "A survey of air-to-ground propagation channel modeling for unmanned aerial vehicles," *IEEE Commun. Surveys Tuts.*, vol. 21, no. 3, pp. 2361–2391, 3rd Quart., 2019.
[8] M. Zolanvari, R. Jain, and T. Salman, "Potential data link candidates for civilian unmanned aircraft systems: A survey," *IEEE Commun. Surveys Tuts.*, vol. 22, no. 1, pp. 292–319, 1st Quart. 2020.
[9] J. Kim, N. Seo, and J. Lee, "Initial UHF band transmission loss measurements for air-to-ground links with maritime path and comparisons with ITU-R models," in *Proc. APISAT*, Dec. 2019, pp. 574–583.
[10] Y. S. Meng and Y. H. Lee, "Measurements and characterizations of air-to-ground channel over sea surface at C-band with low airborne altitudes," *IEEE Trans. Veh. Technol.*, vol. 60, no. 4, pp. 1943–1948, May 2011.
[11] D. W. Matolak and R. Sun, "Air–ground channel characterization for unmanned aircraft systems—Part I: Methods, measurements, and models for over-water settings," *IEEE Trans. Veh. Technol.*, vol. 66, no. 1, pp. 26–44, Jan. 2017.
[12] R. Sun and D. W. Matolak, "Air–ground channel characterization for unmanned aircraft systems—Part II: Hilly and mountainous settings," *IEEE Trans. Veh. Technol.*, vol. 66, no. 3, pp. 1913–1925, Mar. 2017.
[13] D. W. Matolak and R. Sun, "Air–ground channel characterization for unmanned aircraft systems—Part III: The suburban and near-urban environments," *IEEE Trans. Veh. Technol.*, vol. 66, no. 8, pp. 6607–6618, Aug. 2017.
[14] Z. Cui, C. Briso-Rodríguez, K. Guan, C. Calvo-Ramírez, B. Ai, and Z. Zhong, "Measurement-based modeling and analysis of UAV air-ground channels at 1 and 4 GHz," *IEEE Antennas Wireless Propag. Lett.*, vol. 18, no. 9, pp. 1804–1808, Sep. 2019.
[15] Z. Cui, C. Briso-Rodriguez, K. Guan, I. Guvenc, and Z. Zhong, "Wideband air-to-ground channel characterization for multiple propagation environments," *IEEE Antennas Wireless Propag. Lett.*, vol. 19, no. 9, pp. 1634–1638, Sep. 2020.
[16] Z. Cui, C. Briso-Rodríguez, K. Guan, Z. Zhong, and F. Quitin, "Multi-frequency air-to-ground channel measurements and analysis for UAV communication systems," *IEEE Access*, vol. 8, pp. 110565–110574, 2020.
[17] J. Rodríguez-Piñeiro, T. Domínguez-Bolaño, X. Cai, Z. Huang, and X. Yin, "Air-to-ground channel characterization for low-height UAVs in realistic network deployments," *IEEE Trans. Antennas Propag.*, vol. 69, no. 2, pp. 992–1006, Feb. 2021.
[18] X. Cai, T. Izydorczyk, J. Rodríguez-Piñeiro, I. Z. Kovács, J. Wigard, F. M. L. Tavares, and P. E. Mogensen, "Empirical low-altitude air-to-ground spatial channel characterization for cellular networks connectivity," *IEEE J. Sel. Areas Commun.*, vol. 39, no. 10, pp. 2975–2991, Oct. 2021.
[19] N. Schneckenburger, T. Jost, D. Shutin, M. Walter, T. Thiasiriphet, M. Schnell, and U.-C. Fiebig, "Measurement of the L-band air-to-ground channel for positioning applications," *IEEE Trans. Aerosp. Electron. Syst.*, vol. 52, no. 5, pp. 2281–2297, Oct. 2016.
[20] N. H. Ranchagoda, K. Sithamparanathan, M. Ding, A. Al-Hourani, and K. M. Gomez, "Elevation-angle based two-ray path loss model for air-to-ground wireless channels," *Elsevier Veh. Commun.*, vol. 32, pp. 100393–100404, Dec. 2021.
[21] K. Mao, Q. Zhu, M. Song, H. Li, B. Ning, G. F. Pedersen, and W. Fan, "Machine-learning-based 3-D channel modeling for U2V mmWave communications," *IEEE Internet Things J.*, vol. 9, no. 18, pp. 17592–17607, Sep. 2022.
[22] D. Matolak and R. Sun, "Air-ground channel measurements and modeling for UAS," *IEEE Aerosp. Electron. Syst. Mag.*, vol. 29, no. 11, pp. 30–35, Nov. 2014.
[23] *Calculation of Free-Space Attenuation*, document Rec. ITU-R P.525-4, International Telecommunication Union, Aug. 2019.
[24] *Reflection From the Surface of the Earth*, document Rec. ITU-R P.1008-1, International Telecommunication Union, 1990.
[25] R. E. Collin, *Antennas and Radiowave Propagation*, 1st ed. New York, NY, USA: McGraw-Hill, 1985.
[26] A. W. Doerry, "Earth curvature and atmospheric refraction effects on radar signal propagation," Sandia Nat. Laboratories, Albuquerque, NM, USA, Tech. Rep. SAND2012-10690, Jan. 2013.
[27] J. D. Parsons, *The Mobile Radio Propagation Channel*, 2nd ed. Hoboken, NJ, USA: Wiley, 2000.
[28] *A Propagation Prediction Method for Aeronautical Mobile and Radionavigation Services Using the VHF, UHF and SHF Bands*, document Rec. ITU-R P.528-5, International Telecommunication Union, Sep. 2021.
[29] M. Rice, A. Davis, and C. Bettweiser, "Wideband channel model for aeronautical telemetry," *IEEE Trans. Aerosp. Electron. Syst.*, vol. 40, no. 1, pp. 57–69, Jan. 2004.
[30] Q. Lei and M. Rice, "Multipath channel model for over-water aeronautical telemetry," *IEEE Trans. Aerosp. Electron. Syst.*, vol. 45, no. 2, pp. 735–742, Apr. 2009.

JAESIN KIM received the B.S. and M.S. degrees in electrical engineering from Korea University, Seoul, South Korea, in 2008 and 2010, respectively, where he is currently pursuing the Ph.D. degree. Since 2010, he has been a Senior Researcher with the Agency for Defense Development, Daejeon, South Korea. His research interests include signal processing and optimization technologies for the next-generation airborne and spaceborne wireless networks. He received the Best Paper Award from the 18th Asia-Pacific Conference on Communications, in 2012, and the Joint Conference on Satellite Communications, in 2021.

INKYU LEE (Fellow, IEEE) received the B.S. degree (Hons.) in control and instrumentation engineering from Seoul National University, Seoul, South Korea, in 1990, and the M.S. and Ph.D. degrees in electrical engineering from Stanford University, Stanford, CA, USA, in 1992 and 1995, respectively. From 1995 to 2002, he was a member of the Technical Staff with Bell Laboratories, Lucent Technologies, Murray Hill, NJ, USA, where he studied high-speed wireless system designs. Since 2002, he has been with Korea University, Seoul, where he is currently a Professor with the School of Electrical Engineering. He was the Department Head of the School of Electrical Engineering, Korea University, from 2019 to 2021. In 2009, he was a Visiting Professor with the University of Southern California, Los Angeles, CA, USA. He has authored or coauthored more than 200 journal articles in IEEE publications and holds 30 U.S. patents granted or pending. His research interests include digital communications and signal processing techniques applied for next-generation wireless systems. He was elected as a member of the National Academy of Engineering of Korea, in 2015. Currently, he is the Director of "Augmented Cognition Meta-Communication" ERC Research Center Awarded from the National Research Foundation of Korea. He was a recipient of the IT Young Engineer Award from the IEEE/IEEK Joint Award, in 2006, the Best Paper Award from the IEEE Vehicular Technology Conference, in 2009, the Best Research Award from the Korean Institute of Communications and Information Sciences, in 2011, the Best Paper Award from the IEEE International Symposium on Intelligent Signal Processing and Communication Systems in 2013, the Best Young Engineer Award from the National Academy of Engineering of Korea, in 2013, and the Korea Engineering Award from the National Research Foundation of Korea, in 2017. He served as an Associate Editor for the IEEE TRANSACTIONS ON COMMUNICATIONS, from 2001 to 2011, and the IEEE TRANSACTIONS ON WIRELESS COMMUNICATIONS, from 2007 to 2011. He was the Chief Guest Editor of the IEEE Journal on Selected Areas in Communications Special Issue on 4G Wireless Systems, in 2006. He also serves as the Co-Editor-in-Chief for the JOURNAL OF COMMUNICATIONS AND NETWORKS. He is also a Distinguished Lecturer of IEEE.